ACS Energy LETTERS

Cite This: ACS Energy Lett. 2018, 3, 2349−2356

http://pubs.acs.org/journal/aelccp

LETTER

Plasmonic Core−Shell Zirconium Nitride−Silicon Oxynitride Nanoparticles

Stephen Exarhos,[†] Alejandro Alvarez-Barragan,[†] Ece Aytan,[‡] Alexander A. Balandin,[‡,§] and Lorenzo Mangolini*[,†,‡]

[†]Mechanical Engineering Department, Bourns College of Engineering, University of California, Riverside 92521, United States

[‡]Materials Science & Engineering Program, Bourns College of Engineering, University of California, Riverside 92521, United States

[§]Department of Electrical & Computer Engineering, Bourns College of Engineering, University of California, Riverside 92521, United States

Supporting Information

ABSTRACT: We discuss the synthesis and properties of plasmonic zirconium nitride nanocrystals produced using a nonthermal plasma reactor. The process enables the continuous conversion of chemical precursors into free-standing ∼10 nm diameter nanoparticles. Oxidation limits the resonant plasmon energy from ∼2.6 eV for ideal unoxidized particles to ∼2.1 eV for particles exposed to air at room temperature. A simple modification to the plasma process allows the in-flight growth of a conformal silicon oxynitride shell onto the zirconium nitride core. The shell inhibits the oxidation of the core, resulting in particles with a plasmon energy of 2.35 eV. These particles show good plasmonic behavior even after annealing in air at 300 °C, largely improved when compared to unprotected particles that oxidize and lose plasmonic activity at the same temperature. This work represents a step toward the development of earth-abundant, thermally and chemically resistant nanoparticles that can offer an inexpensive alternative to gold and silver and extended applicability in harsh environments.

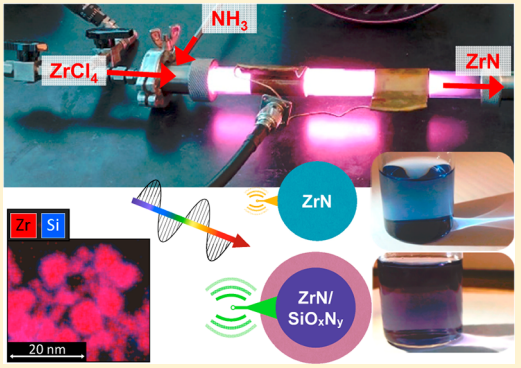

Localized surface plasmon resonance (LSPR) has garnered interest in a variety of fields such as photocatalysis,[1] photovoltaics,[2] solar thermophotovoltaics,[3] biophotonics,[4] and sensing.[5−7] Gold and silver nanostructures have been applied in all of the fields mentioned above because of the ease with which they can be produced at the lab scale.[8,9] However, concerns related to cost, material abundance, and thermal stability motivate the search for alternative plasmonic materials. Among such alternatives, group IVB transition-metal nitrides, such as titanium nitride (TiN), zirconium nitride (ZrN), and hafnium nitride (HfN), show particular promise.[10,11] These materials have been well studied in hard-coating applications due to their high thermal stability and ceramic-like mechanical properties. They exhibit metal-like optical and electronic properties and show LSPR in the visible spectrum if produced in a nanoparticle or nanostructure format.[12−15]

While group IVB metal nitride films can be produced by techniques such as sputtering and chemical vapor deposition,[16−20] their synthesis in nanoparticle form is challenging. For the case of TiN, which to date has attracted the most attention from this class of materials, proposed nanoparticle synthesis approaches include the nitridation of TiO_2 powders[21] or laser ablation of TiN powder targets,[22] both of which have limitations with respect to material yield and particle size distribution control.

ZrN nanoparticles have so far attracted significantly less attention than TiN nanoparticles. Reinholdt et al. used laser ablation of a compacted ZrN target in a N_2 atmosphere to produce monodisperse ZrN nanoparticles with sizes less than 10 nm.[23] These particles were not free-standing but deposited directly onto a silica substrate. Optical characterization revealed a plasmonic resonance within the visible spectrum.[23] ZrN nanoparticles have also been made by zirconium wire explosion in a nitrogen atmosphere,[24] by pulsed wire discharge,[25] and by microwave-mediated synthesis.[26] None of these latter three processes succeeded in creating uniform small ZrN nanoparticles, and none of these particles were characterized optically.[24−26]

Recent reports, including that from our own group, suggest that nonthermal plasmas offer a novel approach for the production of plasmonic TiN nanoparticles.[27,28] While these

Received: August 12, 2018
Accepted: September 10, 2018
Published: September 10, 2018

DOI: 10.1021/acsenergylett.8b01478
ACS Energy Lett. 2018, 3, 2349−2356

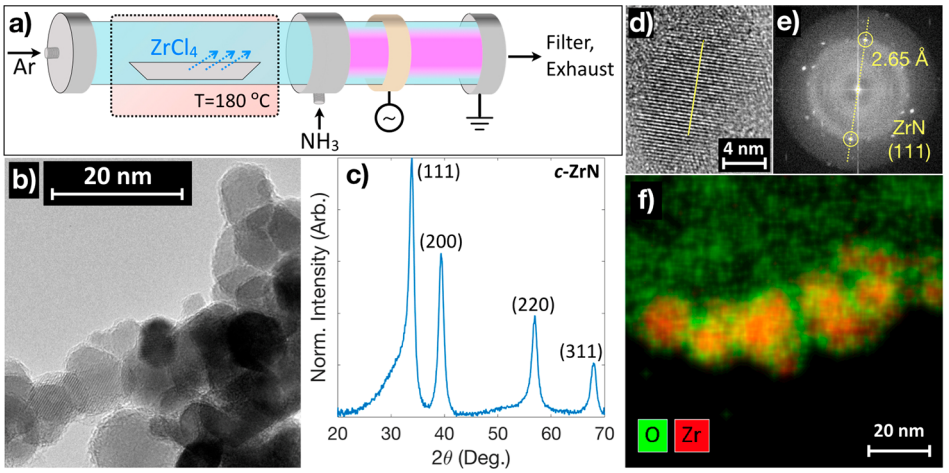

Figure 1. (a) Schematic of the nonthermal plasma system used to synthesize plasmonic ZrN nanoparticles. (b) TEM micrograph of crystalline ZrN nanoparticles. (c) XRD pattern of a sample confirming a cubic ZrN structure. (d) High-resolution STEM image of a single ZrN particle showing crystal lattice fringes and (e) corresponding FFT indicating the standard plane separation aligning with that for the cubic-ZrN(111) plane. (f) STEM-EDS map showing atomic oxygen (green) and zirconium (red) distributions in a selected group of nanoparticles.

reactors were originally developed for the synthesis of silicon quantum dots,[29] several studies confirm that these reactors are compatible with a broad range of materials that include, for example, zinc oxide,[30] silicon carbide,[31] and various metals.[32,33] With this work, we provide evidence that these low-temperature, nonthermal systems are compatible with the synthesis of small ZrN nanoparticles. We have developed a continuous-flow nonthermal plasma process for the nucleation and growth of ZrN nanoparticles starting from zirconium tetrachloride ($ZrCl_4$) and ammonia (NH_3) as precursors. The resulting nanoparticles have a relatively narrow size distribution with size between 5 and 10 nm. They are also free-standing; they are collected as dry powder, which can then be redispersed in a solvent. This opens the possibility of further functionalizing the particles as needed and coating them or printing them onto the surface of interest for various applications.

In this contribution, we describe extensive structural, compositional, and optical characterization of the particles, and we compare the produced material to the theoretically predicted behavior for ZrN nanoparticles. The material characterization, coupled with finite-difference time-domain (FDTD) simulations of the optical cross section of the material, suggests that oxidation plays a significant role in determining the optical response of the ZrN nanoparticles, with oxidation leading to a significant reduction in resonant energy. This conclusion is consistent with previous observations.[23] To address the oxidation issue, we look at previous studies on oxidation in bulk transition-metal nitride coatings.[34−40] One proposed solution involves incorporating nonmetallic elements such as silicon into the material.[37−40] In these ZrN thin films and coatings, silicon tends to form a SiN_x phase, which surrounds the ZrN grains and reduces the rate of oxidation.[38,39] Inspired by this approach, we introduce a second plasma immediately after the ZrN-producing stage to grow, in-flight, a silicon-based protective shell. The coating significantly improves the optical response of the particles by limiting oxidation and the corresponding red shift in LSPR energy. Most importantly, it also improves oxidation resistance at moderately high temperatures in air. This is significant for recent proposals for the control of thermal emission using plasmonic structures, relevant for applications such as thermophotovoltaics.

A schematic of the reactor used here is shown in Figure 1a. The design is based on the scheme commonly utilized for the production of small silicon particles and is very similar to the one that our group has recently used to produce plasmonic TiN nanocrystals.[27] Anhydrous $ZrCl_4$ (Alfa Aesar), NH_3 (AirGas), and Ar are used to nucleate and grow the ZrN nanoparticles. The delivery of the zirconium precursor requires special attention because $ZrCl_4$ has a relatively low vapor pressure and is solid at room temperature.[41] The precursor is placed in an alumina boat inside of a tube furnace upstream of the plasma reactor. The $ZrCl_4$ effective flow rate is controlled by tuning the temperature of the furnace and the reactor pressure (Figure S1). For all samples discussed in this work, the furnace was held at 180 °C and the pressure was 5 Torr. The length of the plasma reactor is 20 cm, and the residence time in the plasma reactor, calculated based on the total gas flow velocity, is 230 ms (Figure S2). NH_3 (10 sccm) is injected into the system downstream of the heated $ZrCl_4$ chamber and allowed to mix with the precursor vapors prior to entering the plasma. The gas mixture is flown through a 2.5 cm diameter quartz tube with a 5 cm wide thin copper plate wrapped around as the electrode. The vacuum flange downstream of the electrode serves as electrical ground, with a distance of ∼12.5 cm separating the downstream edge of the electrode and the ground. The gas is ionized in a 180 W capacitively coupled plasma driven by a 13.56 MHz (RF) power supply. The reaction product is collected downstream on a stainless steel mesh filter. The material as-collected from this system is contaminated by ammonium salts, which are a byproduct of the $ZrCl_{4,(v)}$−NH_3 reaction.[42] These have high vapor pressure and are removed by annealing the powder at 250 °C and 0.30 Torr in 90 sccm of argon flow for 1 h. XRD confirms removal of the ammonium salts during this step (Figure S3). The typical powder production rate is ∼20 mg/h. Details regarding material characterization and FDTD simulations are included in the Supporting Information.

Structural and morphological characterization of a ZrN sample produced under optimized conditions is presented in Figure 1b−f. The TEM micrograph (Figure 1b) shows that the

DOI: 10.1021/acsenergylett.8b01478
ACS Energy Lett. 2018, 3, 2349−2356

crystalline ZrN particles have a generally spherical shape and are fairly monodisperse in size. A particle size distribution was generated from a series of low-magnification TEM images, showing an average particle size of 8.2 nm with a standard deviation of 1.9 nm (Figure S4), which is comparable to that of other nanoparticles produced with a reactor of this type.[27−33] In Figure 1c, the XRD pattern indicates the presence of cubic-phase ZrN. The high-resolution STEM image in Figure 1d and the corresponding fast-Fourier transform (FFT) pattern (Figure 1e) generated from the highlighted region align with standards for the lattice spacing of the ZrN(111) plane.[43]

The diffraction pattern in Figure 1c also indicates some oxidation evidenced by the broad shoulders of the (111) and (220) peaks. Our assignment of this shoulder to an oxidation effect is motivated by additional measurements performed on powder annealed in air at increasing temperature, showing continuous growth of this shoulder relative to the cubic-ZrN diffraction pattern (Figure S5). Additionally, in Figure 1f, a high-resolution EDS map of ZrN particles as-produced from the system shows the distribution of oxygen and zirconium in each particle. Oxygen segregates at the surface of the particles in a conformal shell around a nitrogen- and zirconium-rich core, which explains the apparent amorphous coating on the surface of the particles seen in Figure 1b. The surface oxidation evident in Figure 1 is a result of exposure to air occurring when the samples are extracted from the reactor. While air-free handling of the samples is possible, it is tedious and in our view not as effective as directly growing a protective layer onto the particle surface, as will be discussed later in this Letter.

In Figure S6, we show the elemental composition for five different spots overlapping five particles from the EDS map seen in Figure 1f. We should stress that an exact quantification is challenging because of the small size of the particles and because of the spatial overlapping of particles on top of each other in the image. The measured Zr/N atomic ratio is 1.71 on average, with a large standard deviation of 0.57. This suggests that the particles are not perfectly stoichiometric as produced, likely making them even more oxygen-sensitive. A more detailed analysis of their optical properties provides additional insight into their composition.

Figure 2a shows the optical extinction spectrum for the same sample shown in Figure 1, and the inset shows a photograph of the corresponding dispersion in DI water. There is a clear peak at 585 nm (2.12 eV; fwhm ≈ 0.83 eV) that we attribute to LSPR in the ZrN nanoparticles. Repeated spectroscopic measurements on the same sample yield a deviation in the peak position of 3 nm. The spectrum is repeatable for different samples produced under the same conditions within a deviation of ∼20 nm and moderate deviation in the peak intensity and width using the same operating conditions. In their synthesis of plasmonic ZrN nanoparticles, Reinholdt et al. observed similar optical properties to what we observe: an extinction peak at 653 nm (1.9 eV) with a fwhm of ∼0.8 eV.[23]

In Figure 2b, we provide a comparison of FDTD-simulated optical properties of ideal ZrN nanoparticles (black) and oxidized ZrN nanoparticles (blue). We also include gold nanoparticles (red) for the sake of comparison (all with radii of 5 nm). FDTD models of spherical 5 nm radius ZrN nanoparticles yield a predicted a plasmonic extinction peak at 479 nm (2.58 eV) with a fwhm of ∼0.45 eV. Our experimental data does not conform well to these values, but we are able to reproduce the observed experimental spectrum by modeling a particle with an oxide structure informed by the

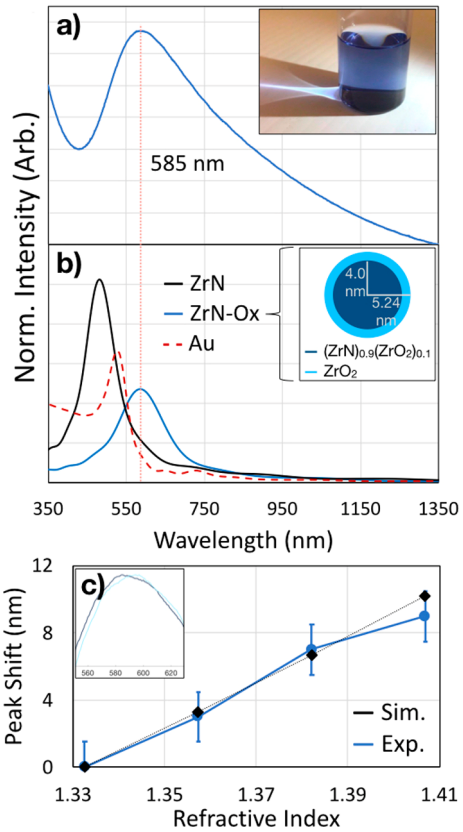

Figure 2. Experimental (a) and simulated (b) optical properties of ZrN nanoparticles. The black curve in (b) corresponds to 5 nm ZrN particles, the dashed red to 5 nm Au particles, and the blue to particles with the oxidation geometry demonstrated in the inset figure. (c) Experimental (blue) and simulated (black) measurements of the shift in peak position with an increasing refractive index of the surrounding medium. The inset in (a) is an image of ZrN particles dispersed in water. The insets in (c) show measured extinction curves from sample dispersed in lowest and highest refractive index solutions.

TEM data in Figure 1. The experimental data is well-modeled using a core−shell particle structure, in which the core consists of a homogeneous mixture of 90% ZrN and 10% ZrO_2 (making $(ZrN)_{0.9}(ZrO_2)_{0.1}$) and the shell consists of pure ZrO_2. The thickness of the shell is adjusted to account for the volume change of a 1 nm thick $(ZrN)_{0.9}(ZrO_2)_{0.1}$ shell transforming into pure ZrO_2 assuming no loss of zirconium atoms, yielding a new shell thickness of 1.24 nm; a schematic of this geometry is shown in the inset to Figure 2b. This composition (atom % Zr = 39.90, atom % N = 19.71, atom % O = 40.39) has a Zr/N ratio of 2.02, in good agreement with the measured stoichiometry from Figure S7.

In order to confirm the plasmonic nature of the extinction peaks shown in Figure 2a, we have monitored the variation in peak position in solvents with varying refractive index.[44,45] We compare the extinction of particles from one ZrN sample dispersed in graded mixtures of DI water (n = 1.333) and ethylene glycol (n = 1.474). The two solvents are miscible, and the refractive index of mixtures of the two solvents trends linearly with the weight fraction of the mixture between that of each pure solvent.[46] Simulations were run using the particle oxidation geometry shown in the inset in Figure 2b with varied medium refractive index surrounding the particle. The experimental samples were all derived from a stock dispersion

DOI: 10.1021/acsenergylett.8b01478
ACS Energy Lett. 2018, 3, 2349−2356

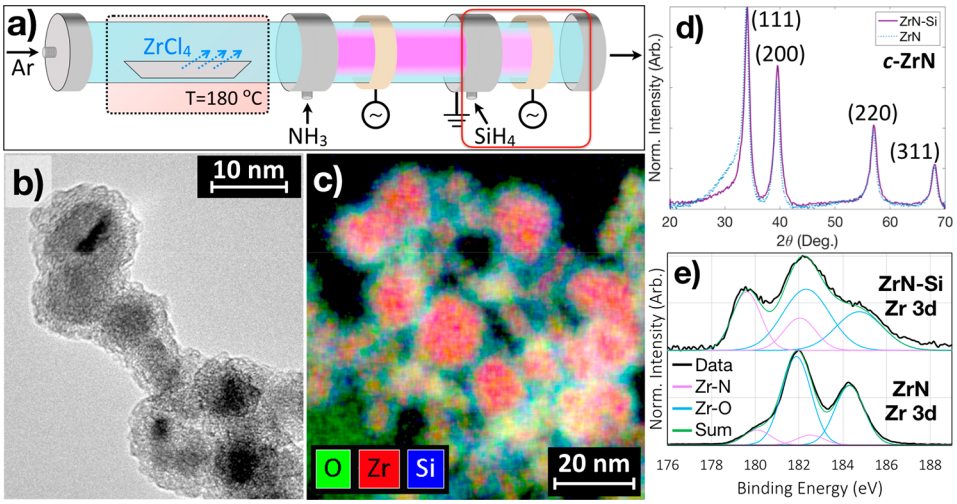

Figure 3. (a) Schematic of the nonthermal plasma system used to synthesize plasmonic ZrN-Si nanoparticles with the addition noted by a red box. (b) TEM micrograph of ZrN-Si nanoparticles. (c) STEM-EDS map showing the atomic oxygen (green), zirconium (red), and silicon (blue) distribution in a selected group of nanoparticles. (d) XRD pattern of the ZrN-Si sample (purple), confirming a cubic ZrN structure with no presence of silicon. Data are overlaid on the pattern for the ZrN sample for comparison. (e) XPS data showing the Zr 3d binding energy for both ZrN-Si (above) and ZrN (below) samples. Fits are included for the Zr−N doublet (purple), Zr−O doublet (blue), and their sum.

of ZrN in DI water. A plot showing both the experimental and simulated extinction peak position as a function of refractive index for 0, 25, 50, and 75 wt % dilutions of ethylene glycol in DI water is shown in Figure 2c. As expected, the extinction peak red shifts with increasing refractive index. Using precious metal nanostructures, a shift in peak position down to 1 nm has been correlated with a shift of 0.006 in refractive index.[45] We observe a weaker dependence for our material, both simulated and experimentally, which we attribute to the dielectric ZrO_2 layer at the surface of the particles. Nevertheless, the good agreement in peak shift between the experimental and the FDTD calculations provides additional validation that our partially oxidized core−oxide shell structure is a reasonably good description of the produced material.

We have also attempted to use these ZrN nanoparticles for surface-enhanced Raman spectroscopy, as shown in Figure S7. We deposited ZrN particles onto a quartz slide and adsorbed Rhodamine 6G (R6G) dye (SigmaAldrich) onto their surface. This molecule is routinely used as a Raman marker.[47] We have monitored the resulting Raman spectra using different excitation wavelengths: 532, 633, and 785 nm. The spectra have been normalized with respect to the laser power to make them comparable. A peak at 1651 cm^{-1} is observed when using the 633 nm probe, which is close to the peak plasmon resonance of the particles. While this measurement provides additional confirmation of the plasmonic nature of the visible extinction band, the quality of the spectra is affected by the fact that only very low incident laser powers could be used, especially for the 633 nm probe. Beam-induced degradation and "burning" has been a serious issue for this measurement, suggesting that this material is likely very effective for photothermal applications.

To summarize, while we do observe LSPR in the ZrN nanoparticles shown here, the behavior is deficient relative to stoichiometric, nonoxidized ZrN nanoparticles of the same size. We attribute this discrepancy to oxidation, a conclusion supported by both the TEM data and by the good agreement between the FDTD calculations and the measured extinction spectra. A novel strategy for the mitigation of the oxidation effects will be described next.

Following from the extensive work studying oxidation and oxidation mitigation in ZrN coatings and films,[39−41,44] we introduce a protective silicon-based coating on the surface of the ZrN particles. This is achieved by injecting silane (SiH_4) gas at 1.4% dilution in argon downstream of the first plasma to initiate the growth of a silicon-containing shell onto the ZrN nanoparticles. The SiH_4 flow is 25 sccm (0.35 sccm SiH_4 accounting for the argon balance), and the second plasma is run at very low RF power (<10 W) to avoid the nucleation of silicon nanoparticles. The material is then collected and annealed to remove NH_4Cl contamination in the same manner as is done for uncoated ZrN nanoparticles. A schematic of the modified system is shown in Figure 3a. For distinction, the silicon-coated particles will henceforth be referred to as ZrN-Si.

Structural and morphological characterization of a representative ZrN-Si sample is shown in Figure 3b−e. The TEM image in Figure 3b shows that the coating is amorphous, conformal, and with a thickness of ∼2 nm. The high-resolution EDS map of ZrN-Si particles in Figure 3c shows the distribution of silicon and oxygen in the shell and a zirconium-rich core with minimal oxygen and silicon.

XRD of a ZrN-Si sample (Figure 3d) confirms that the material is still crystalline ZrN and there is no contribution from crystalline silicon or silicon nitride. In Figure 3d, the diffraction pattern from ZrN-Si (solid purple line) is overlaid on a diffraction pattern from a ZrN sample without the protective shell (dashed blue line), confirming that the crystallite size is negligibly unaffected by the coating process and that the shoulder adjacent to the ZrN (111) peak previously attributed to ZrO_2 is eliminated in the ZrN-Si sample.

Figure 3e shows Zr 3d peaks from XPS spectra of ZrN and ZrN-Si nanoparticles. After subtracting a background calculated by the Tougaard method,[48] the Zr 3d feature is fit with four peaks, accounting for the 3d 5/2 and 3/2 doublets for Zr−O and Zr−N bond energies. The doublet peaks were fit in

DOI: 10.1021/acsenergylett.8b01478
ACS Energy Lett. 2018, 3, 2349−2356

Origin with a Gaussian profile maintaining a standard 2.43 energy difference and a 0.66 peak area ratio between the 5/2 and 3/2 peaks, following the standard procedure as described in prior work.[32] There is significantly less contribution from Zr−O bonds in the ZrN-Si sample relative to the ZrN sample, as indicated by the intensities of the Zr−O peaks (blue curve profiles) relative to the Zr−N peaks (pink curve profiles). The Zr−N peaks in the ZrN sample are also blue-shifted to higher energies than expected from standard values, indicating that the surface-bonding structure is likely closer to N−Zr−O rather than N−Zr−N.[34]

The silicon bonding in the ZrN-Si sample inferred from the fitting of the Si 2p peak (Figure S8) supports the conclusions from prior experiments studying silicon in ZrN coatings and films, namely, that silicon preferentially forms covalent Si−N and Si−O bonds[39,49] (pink and orange lines in Figure S8, respectively) instead of alloying with the ZrN crystal structure.[39] This, along with diffraction and TEM/EDS studies, indicates that the coating does not affect the underlying plasmonic ZrN nanocrystal and is an effective protection technique against oxidation of the plasmonic core.

In Figure 4a, the optical extinction spectrum shows the effect that this coating has on the plasmonic behavior. The photograph of the ZrN-Si powder dispersed in water in the inset of the figure shows that the coating has an effect that is clearly distinguishable even by the naked eye, with the dispersion appearing deep purple in color instead of blue. While we expect the peak to red shift with the introduction of a high refractive index medium on the surface of the plasmonic material ($n \approx 2.02$ for Si_3N_4[50] and $n \approx 1.47$ for SiO_2[51]), the peak is blue shifted to 527 nm (2.35 eV), the intensity is significantly increased when the spectra are normalized to the extinction at 350 nm, and the peak width is reduced to ∼0.66 eV. The ZrN-Si extinction spectrum (solid purple) is overlaid on the theoretical ZrN extinction spectrum (dashed blue line) for comparison, showing that the LSPR is evidently closer to the theoretically predicted behavior with the addition of the coating.

In Figure 4b, we show FDTD-simulated extinction behavior for ideal ZrN (black), oxidized ZrN with the same geometry as that used in Figure 2b (blue), ZrN with a 2 nm $(Si_3N_4)_{0.7}(SiO_2)_{0.3}$ shell (purple, schematic inset), and gold (red) for reference. All simulated particles are 10 nm in diameter with the exception of the ZrN-Si, in which the ZrN core is 10 nm in diameter and the shell is an additional 2 nm thick. While we acknowledge that the shell is an amorphous oxynitride, for simplicity, we model it using the dielectric function for crystalline Si_3N_4 with 30% volume inclusion of SiO_2 generated via the Maxwell-Garnett model.[52,53]

A plot showing both the experimental and simulated extinction peak position as a function of refractive index for 0, 25, 50, and 75 wt % dilutions of ethylene glycol in DI water is shown in Figure 4c. We observe a much weaker LSPR dependence on the surrounding refractive index for ZrN-Si relative to uncoated ZrN. The dependence is also somewhat weaker compared to the theoretical data for the silicon oxynitride structure described earlier (see Figure 4b). A much more detailed and refined treatment of the optical properties of the shell (which, for instance, has amorphous structure while the model uses the optical constants for crystalline silicon oxide and nitride) may lead in the future to a theoretical prediction that is closer to the experimental data.

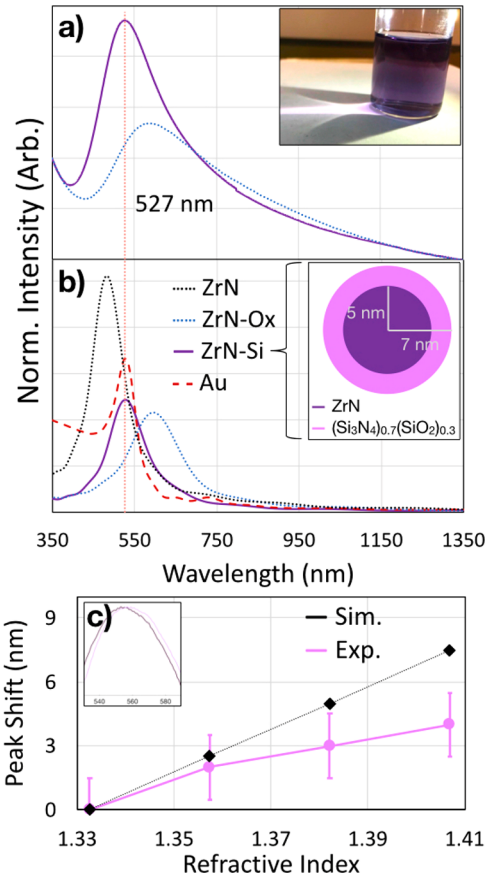

Figure 4. Experimental (a) and simulated (b) optical properties of ZrN-Si nanoparticles (purple lines). In (a), the extinction curve for ZrN is shown (dashed blue line) for comparison. The black curve in (b) corresponds to 5 nm ZrN particles, the dashed red to 5 nm Au particles, blue to particles with the oxidation geometry used in Figure 1, and purple to ZrN-Si particles with structure demonstrated in the inset. (c) Experimental (purple) and simulated (black) measurements of the shift in peak position with an increasing refractive index of the surrounding medium. The inset in (a) is an image of ZrN-Si particles dispersed in water. The inset in (c) shows measured extinction curves from the sample dispersed in lowest and highest refractive index solutions.

Finally, we investigated the stability of our plasma-produced ZrN particles under thermal annealing in air, with the goal of further elucidating the role of the silicon oxynitride shell on the robustness of the material. For this experiment, we started with two batches of ZrN and ZrN-Si powder, split each sample into seven aliquots, and annealed each in air for 1 h at incrementally increasing temperatures. The material was then dispersed in DI water and characterized optically, with the results shown in Figure 5. For ease of comparison, the spectra are normalized at 350 nm, and Figure 5a,b shows both plotted on the same vertical scales.

Figure 5a shows the effect of oxidation on optical extinction in uncoated ZrN nanoparticles. The LSPR is relatively stable even after annealing in air at 150 °C for 1 h. After annealing at higher temperatures, the peak is significantly quenched, until it is completely eliminated after annealing at 400 °C. This sample appears light blue/white, and from XRD, it appears to be crystalline ZrO_2 (Figure S5). Figure 5b shows the same experiment conducted with ZrN-Si nanoparticles. While the initial LSPR for the ZrN-Si particles is already improved from

DOI: 10.1021/acsenergylett.8b01478
ACS Energy Lett. 2018, 3, 2349−2356

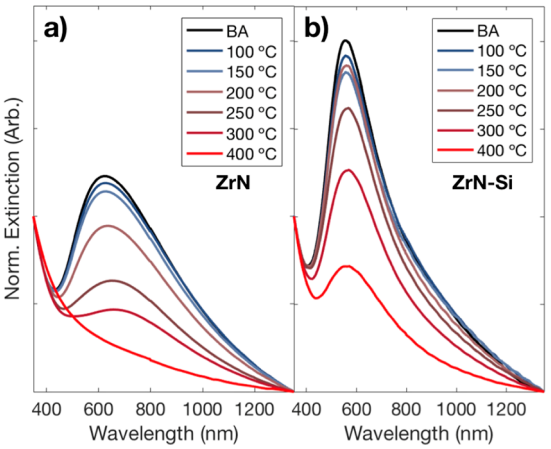

Figure 5. Extinction spectra for ZrN (a) and ZrN-Si (b) particles annealed in air for 1 h at increasing temperatures. Spectra are normalized at 350 nm. The axes are the same for both (a) and (b) for ease of comparison.

that for ZrN, the LSPR is retained under harsher oxidative conditions as well. In fact, the LSPR in ZrN-Si after annealing in air at 300 °C for 1 h approximates the same response from uncoated, nonannealed ZrN particles.

To summarize, we have demonstrated the synthesis of plasmonic ZrN nanoparticles using a nonthermal plasma reactor. Among the advantages of the process are the reasonably high material yield and narrow particle size distribution. It should be stressed that the produced material consists of freestanding particles, making it compatible with further postprocessing and handling in solution. We can produce near-stoichiometric powders, but the produced material is nevertheless sensitive to oxidation. This leads to a plasmon resonance at lower energy than theoretically expected. By leveraging the properties of continuous-flow plasma reactors, we develop a novel approach for protection of the plasmonic particles against oxidation, and we grow a protective silicon-based shell in-flight during material synthesis. This is convenient because it does not affect the overall mass production rate and does not require any additional handling of the material. The core−shell particles have a plasmonic response that matches that of gold nanoparticles of the same size. Most importantly, they showed improved resistance against oxidation in air at moderate temperatures (400 °C). While further engineering of the in-flight coating step will likely provide additional improvements in stability, this work already represents a step toward the development of refractory plasmonic materials with response in the visible spectrum, which is relevant for light management applications at high temperatures and in harsh environments.[3,12,54,55]

■ ASSOCIATED CONTENT

Supporting Information

The Supporting Information is available free of charge on the ACS Publications website at DOI: 10.1021/acsenergylett.8b01478.

Description of material characterization techniques, description of simulation methods, estimated $ZrCl_4$ flow rate based on system parameters, calculated plasma residence time based on system parameters, XRD patterns demonstrating removal of contaminant salts, particle size distribution, XRD patterns and peak position and height trends for ZrN samples annealed at increasing temperatures in air, EDS quantification of ZrN nanoparticle compositions, plot demonstrating SERS on-resonance with ZrN particles, with description of measurement parameters, and Si 2p binding energy region in the XPS spectrum from the ZrN-Si sample (PDF)

■ AUTHOR INFORMATION

Corresponding Author

*E-mail: lmangolini@engr.ucr.edu.

ORCID

Lorenzo Mangolini: 0000-0002-0057-2450

Notes

The authors declare no competing financial interest.

■ ACKNOWLEDGMENTS

This work has been primarily supported by the National Science Foundation under Award No. 1351386 (CAREER). A.A.B. acknowledges support of the "Consejo Nacional de Ciencia y Technologia" (CONACYT, Mexico) and the University of California Institute for Mexico and the United States (UC MEXUS). TEM measurements were performed at the Center for Electron Microscopy and Microanalysis (CFAMM) at UC Riverside. Raman spectroscopy studies in the Balandin group have been supported via NSF award CDSE Collaborative Research: Genetic Algorithm Driven Hybrid Computational−Experimental Engineering of Defects in Designer Materials Award 1404967 and the UC−National Laboratory Collaborative Research and Training Program.

■ REFERENCES

(1) Kale, M. J.; Avanesian, T.; Christopher, P. Direct Photocatalysis by Plasmonic Nanostructures. *ACS Catal.* **2014**, *4*, 116−128.
(2) Clavero, C. Plasmon-Induced Hot-Electron Generation at Nanoparticle/Metal-Oxide Interfaces for Photovoltaic and Photocatalytic Devices. *Nat. Photonics* **2014**, *8*, 95.
(3) Zhou, Z.; Sakr, E.; Sun, Y.; Bermel, P. Solar Thermophotovoltaics: Reshaping the Solar Spectrum. *Nanophotonics* **2016**, *5*, 1−21.
(4) Hirsch, L. R.; Stafford, R. J.; Bankson, J. A.; Sershen, S. R.; Rivera, B.; Price, R. E.; Hazle, J. D.; Halas, N. J.; West, J. L. Nanoshell-Mediated Near-Infrared Thermal Therapy of Tumors under Magnetic Resonance Guidance. *Proc. Natl. Acad. Sci. U. S. A.* **2003**, *100*, 13549−13554.
(5) Nie, S.; Emory, S. R. Probing Single Molecules and Single Nanoparticles by Surface-Enhanced Raman Scattering. *Science* **1997**, *275*, 1102−1106.
(6) Liao, H.; Nehl, C. L.; Hafner, J. H. Biomedical Applications of Plasmon Resonant Metal Nanoparticles. *Nanomedicine* **2006**, *1*, 201−208.
(7) Lal, S.; Link, S.; Halas, N. J. Nano-Optics from Sensing to Waveguiding. *Nat. Photonics* **2007**, *1*, 641.
(8) Daniel, M.-C.; Astruc, D. Gold Nanoparticles: Assembly, Supramolecular Chemistry, Quantum-Size-Related Properties, and Applications toward Biology, Catalysis, and Nanotechnology. *Chem. Rev.* **2004**, *104*, 293−346.
(9) Mock, J. J.; Barbic, M.; Smith, D. R.; Schultz, D. A.; Schultz, S. Shape Effects in Plasmon Resonance of Individual Colloidal Silver Nanoparticles. *J. Chem. Phys.* **2002**, *116*, 6755.
(10) Naik, G. V.; Kim, J.; Boltasseva, A. Oxides and Nitrides as Alternative Plasmonic Materials in the Optical Range. *Opt. Mater. Express* **2011**, *1*, 1090−1099.
(11) Boltasseva, A.; Atwater, H. A. Low-Loss Plasmonic Metamaterials. *Science* **2011**, *331*, 290−291.

DOI: 10.1021/acsenergylett.8b01478
ACS Energy Lett. 2018, 3, 2349−2356

(12) Guler, U.; Shalaev, V. M.; Boltasseva, A. Nanoparticle Plasmonics: Going Practical with Transition Metal Nitrides. *Mater. Today* **2015**, *18*, 227−237.
(13) Lalisse, A.; Tessier, G.; Plain, J.; Baffou, G. Plasmonic Efficiencies of Nanoparticles Made of Metal Nitrides (TiN, ZrN) Compared with Gold. *Sci. Rep.* **2016**, *6*, 38647.
(14) Guler, U.; Naik, G. V.; Boltasseva, A.; Shalaev, V. M.; Kildishev, A. V. Performance Analysis of Nitride Alternative Plasmonic Materials for Localized Surface Plasmon Applications. *Appl. Phys. B: Lasers Opt.* **2012**, *107*, 285−291.
(15) Guler, U.; Suslov, S.; Kildishev, A. V.; Boltasseva, A.; Shalaev, V. M. Colloidal Plasmonic Titanium Nitride Nanoparticles: Properties and Applications. *Nanophotonics* **2015**, *4*, 269−276.
(16) Fix, R.; Gordon, R. G.; Hoffman, D. M. Chemical Vapor Deposition of Titanium, Zirconium, and Hafnium Nitride Thin Films. *Chem. Mater.* **1991**, *3*, 1138−1148.
(17) Wu, D.; Zhang, Z.; Fu, D.; Fan, W.; Guo, H. Structure, Electrical and Chemical Properties of Zirconium Nitride Films Deposited by DC Reactive Magnetron Sputtering. *Appl. Phys. A: Mater. Sci. Process.* **1997**, *64*, 593−595.
(18) Knotek, O.; Münz, W. D.; Leyendecker, T. Industrial Deposition of Binary, Ternary, and Quaternary Nitrides of Titanium, Zirconium, and Aluminum. *J. Vac. Sci. Technol., A* **1987**, *5*, 2173−2179.
(19) Wendel, H.; Suhr, H. Thin Zirconium Nitride Films Prepared by Plasma-Enhanced CVD. *Appl. Phys. A: Solids Surf.* **1992**, *54*, 389−392.
(20) Kurtz, S. R.; Gordon, R. G. Chemical Vapor Deposition of Titanium Nitride at Low Temperatures. *Thin Solid Films* **1986**, *140*, 277−290.
(21) Li, J.; Gao, L.; Sun, J.; Zhang, Q.; Guo, J.; Yan, D. Synthesis of Nanocrystalline Titanium Nitride Powders by Direct Nitridation of Titanium Oxide. *J. Am. Ceram. Soc.* **2001**, *84*, 3045−3047.
(22) Reinholdt, A.; Pecenka, R.; Pinchuk, A.; Runte, S.; Stepanov, A. L.; Weirich, Th. E.; Kreibig, U. Structural, Compositional, Optical and Colorimetric Characterization of TiN Nanoparticles. *Eur. Phys. J. D* **2004**, *31*, 69−76.
(23) Reinholdt, A.; Detemple, R.; Stepanov, A. L.; Weirich, T. E.; Kreibig, U. Novel Nanoparticle Matter: ZrN-Nanoparticles. *Appl. Phys. B: Lasers Opt.* **2003**, *77*, 681−686.
(24) Schlegel, A.; Wachter, P.; Nickl, J. J.; Lingg, H. Optical Properties of TiN and ZrN. *J. Phys. C: Solid State Phys.* **1977**, *10*, 4889.
(25) Sugunakar Reddy, R.; Kamaraj, M.; Kamachi Mudali, U.; Chakravarthy, S. R.; Sarathi, R. Generation and Characterization of Zirconium Nitride Nanoparticles by Wire Explosion Process. *Ceram. Int.* **2012**, *38*, 5507−5512.
(26) Lam, D. V.; Suematsu, H.; Ogawa, T. Characterization of ZrN, ZrO2, and β'−Zr7O11N2 Nanoparticles Synthesized by Pulsed Wire Discharge. *J. Am. Ceram. Soc.* **2017**, *100*, 4884−4892.
(27) Alvarez Barragan, A.; Ilawe, N. V.; Zhong, L.; Wong, B. M.; Mangolini, L. A Non-Thermal Plasma Route to Plasmonic TiN Nanoparticles. *J. Phys. Chem. C* **2017**, *121*, 2316−2322.
(28) Schramke, K. S.; Qin, Y.; Held, J. T.; Mkhoyan, K. A.; Kortshagen, U. R. Nonthermal Plasma Synthesis of Titanium Nitride Nanocrystals with Plasmon Resonances at Near-Infrared Wavelengths Relevant to Photothermal Therapy. *ACS Appl. Nano Mater.* **2018**, *1*, 2869−2876.
(29) Mangolini, L.; Thimsen, E.; Kortshagen, U. High-Yield Plasma Synthesis of Luminescent Silicon Nanocrystals. *Nano Lett.* **2005**, *5*, 655−659.
(30) Thimsen, E.; Johnson, M.; Zhang, A. J.; Wagner, A. J.; Mkhoyan, K. A.; Kortshagen, U. R.; Aydil, E. S. High Electron Mobility in Thin Films Formed via Supersonic Impact Deposition of Nanocrystals Synthesized in Nonthermal Plasmas. *Nat. Commun.* **2014**, *5*, 5822.
(31) Coleman, D.; Lopez, T.; Yasar-Inceoglu, O.; Mangolini, L. Hollow Silicon Carbide Nanoparticles from a Non-Thermal Plasma Process. *J. Appl. Phys.* **2015**, *117*, 193301.
(32) Chiang, W.-H.; Sankaran, R. M. Linking Catalyst Composition to Chirality Distributions of As-Grown Single-Walled Carbon Nanotubes by Tuning Ni_xFe_{1-x} Nanoparticles. *Nat. Mater.* **2009**, *8*, 882−886.
(33) Chiang, W.-H.; Richmonds, C.; Sankaran, R. M. Continuous-Flow, Atmospheric-Pressure Microplasmas: A Versatile Source for Metal Nanoparticle Synthesis in the Gas or Liquid Phase. *Plasma Sources Sci. Technol.* **2010**, *19*, 034011.
(34) Wiame, H.; Centeno, M.-A.; Picard, S.; Bastians, P.; Grange, P. Thermal Oxidation under Oxygen of Zirconium Nitride Studied by XPS, DRIFTS, TG-MS. *J. Eur. Ceram. Soc.* **1998**, *18*, 1293−1299.
(35) Abadias, G.; Koutsokeras, L. E.; Siozios, A.; Patsalas, P. Stress, Phase Stability and Oxidation Resistance of Ternary Ti-Me-N (Me = Zr, Ta) Hard Coatings. *Thin Solid Films* **2013**, *538*, 56−70.
(36) Chen, L.; He, L.; Xu, Y.; Zhou, L.; Pei, F.; Du, Y. Influence of ZrN on Oxidation Resistance of Ti-Al-N Coating. *Surf. Coat. Technol.* **2014**, *244*, 87−91.
(37) Wei, R.; Rincon, C.; Langa, E.; Yang, Q. Microstructure and Tribological Performance of Nanocomposite Ti-Si-C-N Coatings Deposited Using Hexamethyldisilazane Precursor. *J. Vac. Sci. Technol., A* **2010**, *28*, 1126−1132.
(38) Freitas, F. G. R.; Hübler, R.; Soares, G.; Conceição, A. G. S.; Vitória, E. R.; Carvalho, R. G.; Tentardini, E. K. Structural and Mechanical Properties of Zr-Si-N Thin Films Prepared by Reactive Magnetron Sputtering. *Mater. Res.* **2015**, *18*, 30−34.
(39) Saladukhin, I. A.; Abadias, G.; Uglov, V. V.; Zlotski, S. V.; Michel, A.; Janse van Vuuren, A. Thermal Stability and Oxidation Resistance of ZrSiN Nanocomposite and ZrN/SiNx Multilayered Coatings: A Comparitive Study. *Surf. Coat. Technol.* **2017**, *332*, 428−439.
(40) Diéguez, L.; Caballero, D.; Calderer, J.; Moreno, M.; Martínez, E.; Samitier, J. Optical Gratings Coated with Thin Si_3N_4 Layer for Efficient Immunosensing by Optical Waveguide Lightmode Spectroscopy. *Biosensors* **2012**, *2*, 114−126.
(41) Palko, A. A.; Ryon, A. D.; Kuhn, D. W. The Vapor Pressures of Zirconium Tetrachloride and Hafnium Tetrachloride. *J. Phys. Chem.* **1958**, *62*, 319−322.
(42) Yajima, A.; Segawa, Y.; Matsuzaki, R.; Saeki, Y. Reaction Process of Zirconium Tetrachloride with Ammonia in the Vapor Phase and Properties of the Zirconium Nitride Formed. *Bull. Chem. Soc. Jpn.* **1983**, *56*, 2638−2642.
(43) Chieh, Y.-C.; Lo, W.-Z.; Lu, F.-H. Microstructure Evolution of ZrN Films Annealed in Vacuum. *Surf. Coat. Technol.* **2006**, *200*, 3336−3340.
(44) Luther, J. M.; Jain, P. K.; Ewers, T.; Alivisatos, A. P. Localized Surface Plasmon Resonances Arising from Free Carriers in Doped Quantum Dots. *Nat. Mater.* **2011**, *10*, 361.
(45) Mock, J. J.; Smith, D. R.; Schultz, S. Local Refractive Index Dependence of Plasmon Resonance Spectra from Individual Nanoparticles. *Nano Lett.* **2003**, *3*, 485−491.
(46) Tsierkezos, N. G.; Molinou, I. E. Thermodynamic Properties of Water + Ethylene Glycol at 283.15, 293.15, 303.15, and 313.15 K. *J. Chem. Eng. Data* **1998**, *43*, 989−993.
(47) Dong, Z.; Wei, H.; Chen, Y.; Wang, R.; Zhao, J.; Lin, J.; Bu, J.; Wei, Y.; Cui, Y.; Yu, Y. Surface Enhanced Raman Scattering Activity of TiN Thin Film Prepared via Nitridation of Sol-Gel Derived TiO_2 Film. *AOPC 2015: Advanced Display Technology; and Micro/Nano Optical Imaging Technologies and Applications. Proc. SPIE* **2015**, *9672*, 967209.
(48) Repoux, M. Comparison of Background Removal Methods for XPS. *Surf. Interface Anal.* **1992**, *18*, 567−570.
(49) Ténégal, F.; Gheorghiu de la Rocque, A.; Dufour, G.; Sénémaud, C.; Doucey, B.; Bahloul-Hourlier, D.; Goursat, P.; Mayne, M.; Cauchetier, M. Structural Determination of Sintered Si_3N_4/SiC Nanocomposite Using the XPS Differential Charge Effect. *J. Electron Spectrosc. Relat. Phenom.* **2000**, *109*, 241−248.
(50) Philipp, H. R. Optical Properties of Silicon Nitride. *J. Electrochem. Soc.* **1973**, *120*, 295−300.

DOI: 10.1021/acsenergylett.8b01478
ACS Energy Lett. 2018, 3, 2349−2356

(51) Rodriguez-de Marcos, L. V.; Larruquert, J. I.; Méndez, J. A.; Aznárez, J. A. Self-Consistent Optical Constants of SiO_2 and Ta_2O_5 Films. *Opt. Mater. Express* **2016**, *6*, 3622−3687.
(52) Gittleman, J. I.; Abeles, B. Comparison of the Effective Medium and the Maxwell-Garnett Predictions for the Dielectric Constants of Granular Materials. *Phys. Rev. B* **1977**, *15*, 3273−3275.
(53) Ruppin, R. Validity Range of the Maxwell-Garnett Theory. *Phys. Status Solidi B* **1978**, *87*, 619−624.
(54) Zhou, N.; Xu, X.; Hammack, A. T.; Stipe, B. C.; Gao, K.; Scholz, W.; Gage, E. C. Plasmonic Near-Field Transducer for Heat-Assisted Magnetic Recording. *Nanophotonics* **2014**, *3*, 141−155.
(55) Boyd, D. A.; Greengard, L.; Brongersma, M.; El-Naggar, M. Y.; Goodwin, D. G. Plasmon-Assisted Chemical Vapor Deposition. *Nano Lett.* **2006**, *6*, 2592−2597.

DOI: 10.1021/acsenergylett.8b01478
ACS Energy Lett. 2018, 3, 2349−2356